



**HAL**  
open science

## Compressibility effects on Flat-Plates with Serrated Leading-Edges at a Low Reynolds Number

Etienne Mangeol, Ishiwaki Daichi, Wallisky Nicolas, Asai Keisuke, Nonomura Taku

► **To cite this version:**

Etienne Mangeol, Ishiwaki Daichi, Wallisky Nicolas, Asai Keisuke, Nonomura Taku. Compressibility effects on Flat-Plates with Serrated Leading-Edges at a Low Reynolds Number. *Experiments in Fluids*, 2017, 58, pp.159. 10.1007/s00348-017-2443-6 . hal-01667355

**HAL Id: hal-01667355**

**<https://hal.science/hal-01667355>**

Submitted on 19 Dec 2017

**HAL** is a multi-disciplinary open access archive for the deposit and dissemination of scientific research documents, whether they are published or not. The documents may come from teaching and research institutions in France or abroad, or from public or private research centers.

L'archive ouverte pluridisciplinaire **HAL**, est destinée au dépôt et à la diffusion de documents scientifiques de niveau recherche, publiés ou non, émanant des établissements d'enseignement et de recherche français ou étrangers, des laboratoires publics ou privés.



## Open Archive Toulouse Archive Ouverte (OATAO)

OATAO is an open access repository that collects the work of some Toulouse researchers and makes it freely available over the web where possible.

This is an author's version published in: <https://oatao.univ-toulouse.fr/18637>

**Official URL** : <http://dx.doi.org/10.1007/s00348-017-2443-6>

### To cite this version :

Mangeol, Etienne and Daichi, Ishiwaki and Nicolas, Wallisky and Keisuke, Asai and Taku, Nonomura Compressibility effects on Flat-Plates with Serrated Leading-Edges at a Low Reynolds Number. (2017) Experiments in Fluids, vol. 58 (n° 159). pp. 1-14. ISSN 0723-4864

Any correspondence concerning this service should be sent to the repository administrator:

[tech-oatao@listes-diff.inp-toulouse.fr](mailto:tech-oatao@listes-diff.inp-toulouse.fr)

# Compressibility effects on Flat-Plates with Serrated Leading-Edges at a Low Reynolds Number

Étienne Mangeol · Daichi Ishiwaki · Nicolas Wallisky · Keisuke Asai · Taku Nonomura

**Abstract** This study evaluates the influence of a serrated leading edge on flat-plate aerodynamics at low-Reynolds-number and subsonic high-Mach-number conditions. Forces are measured for a Mach number ranging from 0.2 to 0.64 at a Reynolds number of  $(12,000 \pm 1000)$ . Pressure distributions are obtained under the same conditions using pressure sensitive paint (PSP) measurement. Three models are tested: a flat plate without serrations used as the baseline case and two flat plates with serrated leading edges of different wavelength-to-amplitude ratios. Results show that the aerodynamic performance of flat plates with serrations is slightly changed from the baseline case. The plate with short-wavelength serrations underperforms in terms of the lift-to-drag ratio under all the conditions compared to the baseline case while the plate with large-wavelength serrations slightly outperforms it at around the stall angle. The Mach number has little effect on the attached flow while the lift increases with the Mach number under deep stall conditions. Serrations maintain the lift even under high angle of attack conditions when Mach number varies. The two-dimensional pressure distributions and the analyses of local chordwise pressure coefficient distributions at different spanwise locations and of periodicity of spanwise pressure coefficients allow categorisation of the complex flow structures into three types. These configurations feature different types of low pressure regions downstream of troughs. The periodicity of the pattern depends not only on the angle of attack but also on the Mach number.

**Keywords** Serrations · Low Reynolds Number · Compressibility

## 1 Introduction

The development of micro aerial vehicles (MAV) has renewed interest in low Reynolds number flight in the past twenty years (Laitone, 1997). The flow conditions of a Martian airplane proposed by National Aeronautics and Space Administration (NASA) and Japan Aerospace Exploration Agency (JAXA) lie in the same range of low Reynolds numbers as MAVs (Oyama and Fujii, 2006; Guynn et al, 2003). In recent years, biomimetics have also given a new approach to solve the issues raised by flight in these conditions. Humpback whales, owls and dragonflies are three species presenting remarkable aerodynamic features that researchers have tried to understand.

Among those features, one is common to these three species: they possess a serrated leading-edge (SLE) on their flippers or wings. Numerous studies of the humpback whale flippers have been carried out recently (Johari et al, 2007; Miklosovic et al, 2004; Hansen et al, 2011; Van Nierop et al, 2008). The tubercles on their flippers tend to delay stall (Miklosovic et al, 2004; Van Nierop et al, 2008) and to enhance post-stall aerodynamic efficiency. The precise aerodynamic mechanism that leads to these enhancements is still an open issue for discussion.

Studies of the fundamental effect of SLE independently of aerofoil consideration, using a flat plate, have been scarce. Cranston et al (2012) have studied the Reynolds number effect of SLE on models of serrated leading-edge flat plate with the same wavelength used in the present study (however experimental conditions were different from Cranston et al (2012) and a three-dimensional flow was studied). They have shown that SLE had little influence on the lift slope but large serrations increased the stall angle. This might be interesting for MAVs for which

---

Étienne Mangeol  
ISAE-SUPAERO 10 avenue Édouard Belin, 31055, Toulouse, France  
E-mail: etienne.mangeol@supaero.isae.fr

Keisuke Asai · Taku Nonomura · Daichi Ishiwaki · Nicolas Wallisky  
Department of Aerospace Engineering, Tohoku University, 6-6-1 Aoba, Aoba-ku, Sendai, Japan

resistance to gusts is a crucial issue.

Sakai et al (2015) studied the three-dimensional flow structure on serrated leading-edge flat plate by stereo particle image velocimetry at  $Re = 5.0 \times 10^3$ . They observed the generation of counter-rotating vortices in reverse-flow areas and multiple patterns of merging of peaks' flows. They proposed a categorisation of flow patterns. A basic understanding of the flow mechanism has been presented by Dropkin (Dropkin et al, 2012) who carried out a numerical simulation of SLE aerofoils NACA 63<sub>4</sub>-021 and described the pressure distribution. He points out that the pressure downstream of the troughs is lower than that on the peaks and that the pressure recovery is quicker downstream of these troughs, leading to an early stall of these regions while the peaks remain attached.

The purpose of this study is to determine the effect of compressibility on a flat plate with a serrated leading-edge. Mars airplane concepts have a cruise speed of Mach 0.4 - 0.5 meaning that the flow on their wings is in the high-subsonic flows area. Furthermore, NASA is considering an airplane with a propeller on which tip speed reaches the speed of sound and in this domain, compressibility is an important feature that can affect both performance and flow configuration (NASA also considers the development of a helicopter UAV for Mars which raises the same issues). The Mars Wind Tunnel (MWT) in Tohoku University (Anyoji, 2011) is used to reach a high subsonic Mach number condition while keeping a low Reynolds number of approximately 12,000. Aerodynamic forces are measured using a three-component balance system while pressure-sensitive paint (PSP) is used to assess the pressure distribution. The evaluation of force coefficients gives insight into the effect of compressibility on SLE flat plates. The pressure distribution is used to visualise the effect of the flow structure impacting the plate and its alteration with rising angle of attack or Mach number. Analyses of spanwise periodicity and local chordwise pressure coefficient curves are carried out to complete the two-dimensional pressure distribution in order to build a system to categorise the flow structures.

## 2 Pressure-Sensitive Paint

### 2.1 Stern-Volmer Equation

Pressure-sensitive paint is a commonly used coating sensor that provides the pressure distribution on an aerofoil. It is particularly well adapted to thin aerofoils (Liu and Sullivan, 2005) on which it is difficult to install many pressure taps. Detailed explanations of PSP measurement techniques can be found in Liu and Sullivan (2005). The relation between luminescence intensity and pressure is known as the Stern-Volmer relation:

$$\frac{I_{\text{ref}}}{I} = A(T) + B(T) \frac{P}{P_{\text{ref}}}$$

Here,  $A$  and  $B$  are coefficients determined by calibration test while  $I_{\text{ref}}$  and  $I$  are obtained by taking pictures during wind-on and wind-off conditions, respectively. The subscript "ref" represents the quantity in the reference (wind-off) condition.

The PSP used in the MWT is demonstrated to have a high pressure sensitivity below 14 kPa (Mori et al, 2004). It is composed of 4.8 mg of palladium tetra(pentafluorophenyl) porphyrin (PdTFPP) as the active molecule and of 0.16 g of poly[1-(trimethylsilyl)-propyne] [poly(TMSP)] as the polymer binder in 20 mL of toluene as solvent. The absorption peak is located at 407 nm and the emission peak at 670 nm (Anyoji, 2011). The pressure sensitivity is demonstrated to be 10% /kPa at a pressure around 5 kPa.

The calibration test is conducted in the test-section during evacuation at each angle of attack test. This method provides the calibration coefficients for each pixel of the image so that nonuniformity in pressure sensitivity is corrected.

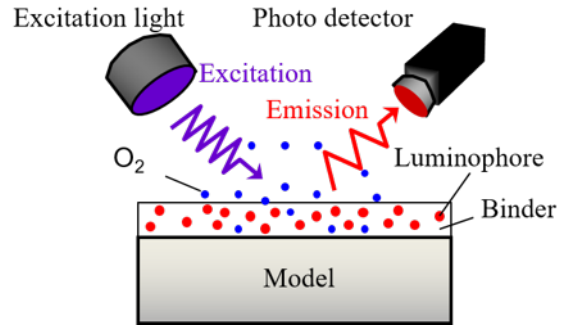


Fig. 1 PSP measurement principle

### 2.2 Temperature Calibration

The PSP used is considered ideal, meaning that  $A_{\text{ref}}(T)$  and  $B_{\text{ref}}(T)$  are independent of temperature. The Stern-Volmer relation can then be written (Yamashita et al, 2007):

$$\frac{I_{\text{ref}}}{I} = k(T) \left[ A_{\text{ref}} + B_{\text{ref}} \frac{P}{P_{\text{ref}}} \right]$$

With,  $A_{\text{ref}}$  and  $B_{\text{ref}}$  obtained by *in-situ* calibration.

The high temperature conductivity of the aluminium model and the short test-time (less than 30 seconds) ensure the uniformity of the temperature distribution, so that  $k$  is uniform on the whole wing (Anyoji, 2011).

This coefficient  $k(T)$  is obtained by *a priori* calibration in a calibration chamber and by a one-point measurement directly on the aerofoil with a thermocouple. See Anyoji et al (2015) for details about this temperature calibration.

### 3 Experimental Setup

#### 3.1 Mars Wind Tunnel

The MWT can be divided into three main components: an induction-type tunnel, a vacuum chamber and a buffer tank. The tunnel is located inside the vacuum chamber, allowing simulation the low Martian atmospheric pressure. The pressure is kept constant during tests by adjusting the position of a butterfly valve on a pipe connecting the vacuum chamber to the buffer tank. The flow is driven by an ejector nozzle placed downstream of the test section. This test section is 100 mm wide and 150 mm high. Details of the facility can be found in Anyoji (2011) or Anyoji et al (2009) and a schematic is presented in Figure 2.

The unique feature of this facility is that it can reach a high subsonic Mach number (up to 0.7) while keeping a low Reynolds number. The Mach and Reynolds numbers can be modified independently, allowing studies of pure Reynolds or Mach numbers effects. There are five screens and a honeycomb at the tunnel inlet to reduce turbulence. The flow quality through the Mars Wind Tunnel's operational envelope has been thoroughly described by Anyoji (2011). In particular, the wall boundary layers' size is lower than 11 mm in their experiments at  $Re = 3,300$ . Given that the boundary layers' size decrease with increasing Mach number, their size in the present experiments is slightly lower.

#### 3.2 Models

Three models are tested. They all have a mean aerodynamic chordlength of  $c = 50$  mm and a full test section span with a 0.1 mm gap on either side. They are made out of a 1 mm-thick aluminium (5052-O) thin plate, corresponding to a relative thickness of 2%. The leading edges are square. The models are:

- A blunt flat plate (PP1) used as a reference to compare to the serrated models.

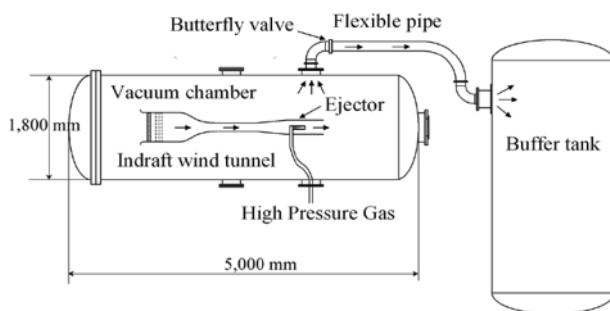


Fig. 2 Schematic of the Mars Wind Tunnel

- A serrated leading edge blunt flat plate (PP2) with serrations shaped as isosceles triangles. The amplitude of the serrations is  $A = 2.5$  mm ( $A/c = 0.05$ ) and wavelength is  $\lambda = 6.24$  mm ( $\lambda/A = 2.5$ ). The wavelength of this model corresponds to that of the S2 model (medium serrations) tested by Cranston et al (2012).
- Another serrated leading edge blunt flat plate (PP3). The amplitude of the serrations is kept constant at  $A = 2.5$  mm but the wavelength is half that of PP2,  $\lambda = 3.12$  mm ( $\lambda/A = 1.25$ ). The wavelength of the model corresponds to the S3 model (small serrations) tested by Cranston et al (2012).

As the mean aerodynamic chord is kept constant, the reference area is the same for the three models. The design of the wings is presented in Figure 3. For force experiments, clean models, without pressure tubes are used. For PSP experiments, a thermocouple is placed under the wing to correct the temperature sensitivity of PSP. Models are also equipped with a pressure tube connected to the pressure tap in order to conduct *in-situ* calibration of the PSP pressure measurement in addition to *a priori* calibration. The models being extremely thin, pressure tubes had to be placed outside the wings. Another blunt flat plate (PP4) with a leading edge similar to PP1 but without pressure tube has also been tested (the trailing edge serrations do not appear to alter significantly the pressure distribution at the location of the leading edge separation bubble). This model is investigated for clarifying the asymmetric pressure distribution. As discussed later, comparison of PP1 and PP4 results shows that the pressure distributions of the half side of the wing surface which is far from the pressure tube are hardly changed by the pressure tube and this side can be used for the quantitative discussion.

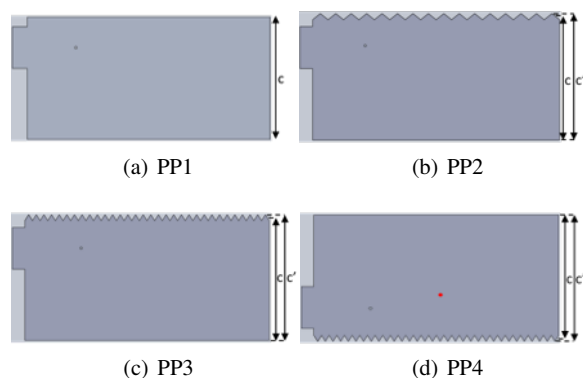
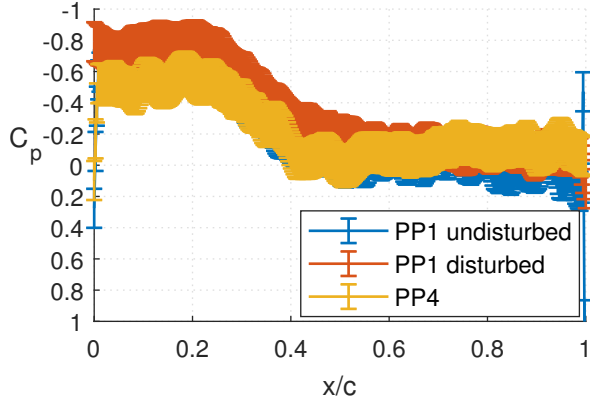


Fig. 3 Test models



**Fig. 4** Chordwise  $C_p$  distribution of PP1 and a flat plate without pressure tube at  $\alpha = 4^\circ$  at  $M = 0.20$  &  $Re = 12,000$

### 3.3 Experimental Conditions

In order to evaluate the Mach number effect alone, the Reynolds number is fixed at approximately 12,000 (11,000-13,000). The Mach number is varied between 0.2 and 0.64. The Reynolds and Mach numbers are changed independently by setting the total pressure ( $P_t$ ) in the vacuum chamber and the supply pressure ( $P_{sup}$ ) of the ejector. [Table 1](#) summarises the experimental conditions adopted in the present study. For force experiments, the angle of attack ( $\alpha$ ) is varied from  $-4^\circ$  to  $25^\circ$  and is basically increased by an increment of  $2^\circ$ . The angle of attack is varied in finer increments around  $7^\circ$  with increment of  $1^\circ$ . The angle of attack of  $7^\circ$  is the stall angle in the blunt flat plate experiment of Anyoji (2011) that was conducted in the reference condition 1 with a flat plate with a 5% relative thickness based on the chord length. The range is extended to  $25^\circ$  compared to this reference experiment to match the range chosen by Cranston et al (2012) and to be able to observe the serrations effect in deep stall conditions. A  $5^\circ$ -step was used in the deep stall region for  $\alpha$  greater than  $15^\circ$ .

**Table 1** Experimental conditions

	$Re$	$M$	$P_t$ (kPa)	Run Time (s)
Condition 1 (Ref)	12,000	0.2	5	60
Condition 2	11,000	0.46	3	20
Condition 3	13,000	0.64	1.8	10

Condition 1 is used by Anyoji (2011) and serves as reference condition. Condition 2 corresponds to the Mach number in the work of Oyama and Fujii (2006). Condition 3 corresponds to requirements of Mars airplane according to Guynn et al (2003).

### 3.4 Force experiments

A three-component balance system is used to measure the forces on the models. Forces were measured without wind (wind-off) and wind on. The measurements without wind were subtracted from those with wind on in order to remove the weight of the model and capture only the lift and drag. During balance calibration an influence matrix of the drag on the lift measurement is obtained and this influence is removed during the lift computation.

The walls' effect on the flow was taken into account. It can be divided into the side-walls' effect and the lower/upper walls' effect. For the former one, a clearance of 0.1 mm is kept between the model and the tunnel walls. This clearance gap is smaller than 0.5% of the wing span, so that the effect of the side walls can be neglected as explained by Anyoji (2011). For the upper and lower walls' effect, the pressure gradient is corrected by a gradual increase of the section area while blockage and upwash effects were corrected following the method described in Pankhurst and Holder (1952).

Errors in the force measurement have three main sources: the uncertainty of the balance, the pitch angle setting and the dynamic pressure uncertainty. These were evaluated as follows:

- The Full Scale (FS) error of the load cells was 0.021% FS on lift and 0.015% FS on drag.
- The specification of the angle motor gives the accuracy obtained on the angle of attack. This then disturbs the drag measurement. Pitching accuracy of the motor:  $d\alpha = 3.4 \cdot 10^{-2}$  (deg)  
Influence on drag:  $d\text{Drag} = \text{Lift} \cdot \sin(d\alpha)$  (N)
- The dynamic pressure ( $q$ ) was computed from the density and the flow speed. So we can compute the dynamic pressure error depending on the errors on density and velocity measurements with the formula:  $dq/q = d\rho/\rho + 2 \cdot dv/v$   
The errors on density and velocity were determined from their variation during the experiment time. So, at  $M = 0.2$ , we have  $dq/q = 2.9\%$ , at  $M = 0.46$   $dq/q = 1.7\%$  and at  $M = 0.64$   $dq/q = 1.1\%$ .

Those errors were summed to plot the global error on force measurements and tend to be rather small. Furthermore, measurements in each condition were carried out twice in order to ascertain their repeatability. Each time the data was perfectly consistent so that it gives sufficient reliability on the results.

### 3.5 PSP Experiments

#### 3.5.1 Optical Setup

A schematic of the optical set up for the PSP experiments is presented in [Figure 5](#). Two ultra-violet light-emitting diodes (UV-LED) with 400 nm wavelength were

used to provide excitation light. Images were captured by a 16-bit digital complementary metal-oxide semiconductor (C-MOS) camera (Hamamatsu C11440-22CU, ORCA Flash 4.0) with a bandpass filter centred on 670 nm ( $\pm 20$  nm) and a f2.8 lens (Nikon, 105mm).

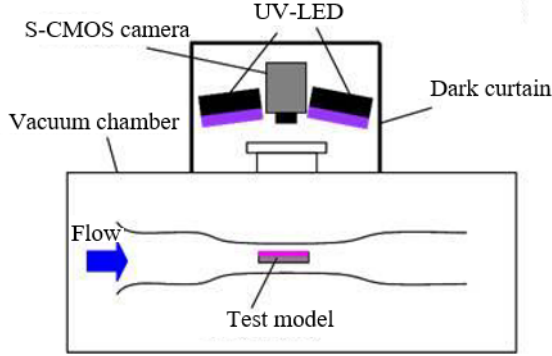


Fig. 5 Schematic of MWT optical set up

### 3.5.2 Image Processing

The image processing is described as follows:

1. Subtraction of dark images  $I_{\text{dark}}$  from  $I_{\text{ref}}$  and  $I_{\text{run}}$  to remove dark current noise and stray light.
2. Averaging of images  $I_{\text{ref}}$  taken during the wind-off condition and  $I_{\text{run}}$  taken during the wind-on condition. Thirty images are averaged for wind-off images, while the number of averaged wind-on images is six to forty three depending on the experimental conditions.
3. Registration of images. Marker points are placed on the model before testing. Aligning their positions between the wind-off and wind-on conditions corrects model movement.
4. Computation of the intensity ratio  $I_{\text{ref}}/I_{\text{run}}$ .
5. Calculation of the pressure distribution with the Stern-Volmer relation taking into account the measured temperature.

The pressure obtained is further corrected with an offset given by the precise pressure measurement from the pressure tap with a Baratron pressure sensor (model number 627B 12T with an error of 0.12% of read value). This procedure is corresponding to the hybrid *a priori* and *in-situ* calibration.

The uncertainties on the measured pressure depend on the number of images taken during the test. They have two sources:

- The camera shot noise which can be accessed by the full-well capacity of the C-MOS ORCA 4.0 camera used. From this, the uncertainty on the measured intensity can be calculated. This uncertainty depends on the number of images averaged during the experiments which itself

depends on the Mach number of the flow. Then the uncertainty on the pressure measurement is evaluated through the Stern-Volmer relation.

- The temperature changes which affect mostly the level of absolute pressure. As we use a pressure tap, this error is as small as the uncertainty on the pressure scanner which is given by its specifications as a static error of 0.0085kPa.

They vary between  $dP = 40$  Pa at  $M = 0.2$ ,  $dP = 44$  Pa at  $M = 0.46$  and  $dP = 97$  Pa at  $M = 0.64$ .

## 4 Results and Discussion

### 4.1 Force Experiments

The data from the reference flat plate are plotted with data from Anyoji (2011) and Okamoto et al (1996) the works of whom both feature thin flat plates at the same Reynolds number of  $1.1 - 1.2 \times 10^4$ , and the measurement accuracy is validated. Figure 6 shows that our measurements follow closely those of Okamoto et al (1996). In this figure the angle of attack is not corrected to take into account the blockage and upwash effects because Anyoji and Okamoto did not correct those effects. In all the other figures, the angle of attack and force coefficients have been corrected, this is signalled by the subscript *corr*. The flat plate of Anyoji (2011) is thicker and the slope  $dC_l/d\alpha$  is slightly steeper than that of the present study, as expected from the conclusions of Okamoto et al (1996) on the effects of the flat-plate thickness. On the other hand,  $C_{l_{\text{max}}}$  is greater in the experiment of Anyoji (2011) which is contradictory with the conclusions of Okamoto et al (1996) that the thicker the flat plate is, the lower the  $C_{l_{\text{max}}}$  should be.

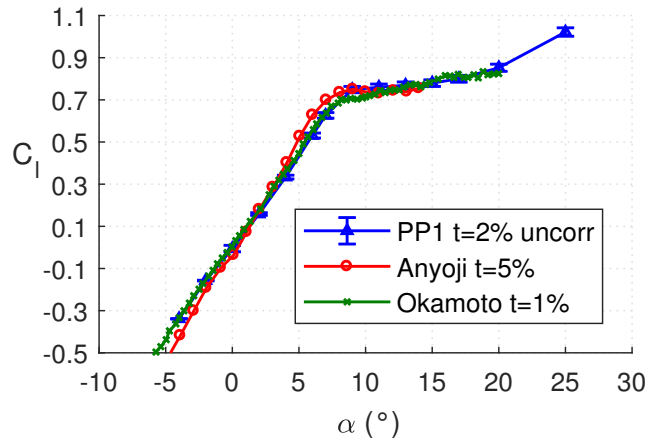


Fig. 6 Validation of force measurements

4.1.1 Serrations influence in reference case ( $Re=12,000, M=0.2$ )

The effect of the serrated leading edge on  $C_l$  in the condition of a Reynolds number of 12,000 and a Mach number of 0.2 is clearly illustrated in Figure 7: the large serrations on PP2 increase the corrected stall angle to approximately  $7^\circ$  instead of  $5^\circ$  for the basic flat plate PP1. The  $C_l$  around the stall is similar to PP1. On the other hand, PP3, which has smaller serrations, shows a globally worse  $C_l$  performance. The stall of PP3 occurs at the same angle of attack as that of PP1 but the lift coefficient of PP3 is 7.5% lower than that of PP1.

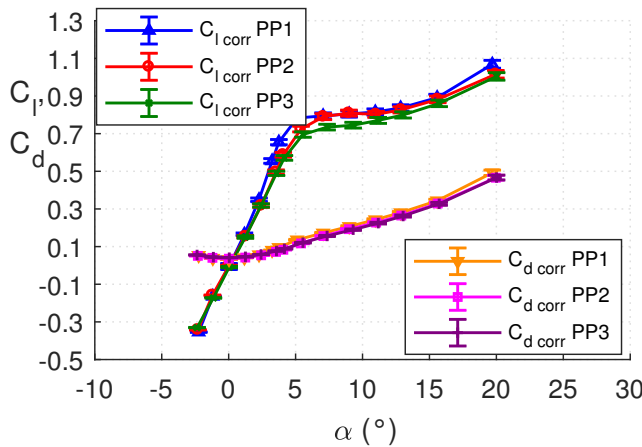


Fig. 7 Lift and Drag curves in condition 1

The drag coefficient curves of Figure 7 point out that the serrations of both PP2 and PP3 slightly reduce drag compared to PP1 (for an angle of attack between  $3^\circ$  and  $9^\circ$  this reduction amounts to 5%-13% of the  $C_{l,corr}$  compared to PP1). Although the reduction in drag by serrations is an expected result for PP3, the lift of which is lower than that of PP1, it is an interesting result for PP2 which displays a similar lift to PP1 from  $7^\circ$  until  $15^\circ$ .

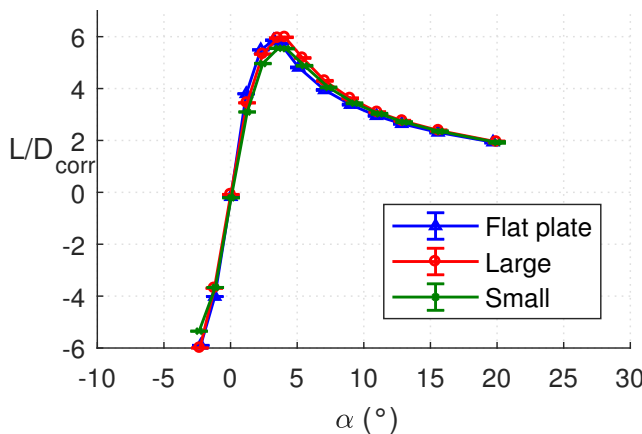


Fig. 8 Lift-to-drag ratio curves in condition 1

Finally, the lift-to-drag ratio curves in Figure 8 show that the performance of PP3 is the worst on the majority of the range of angles of attack explored, it is only slightly superior to PP1 after stall (for angles of attack between  $7^\circ$  and  $13^\circ$  the  $L/D_{corr}$  of PP3 is 1-2% superior to the one of PP1). The maximum of the lift-to-drag ratio curve of PP2 is reached at a angle of attack of  $4.1^\circ$ , which is  $0.9^\circ$  higher than that of PP1, with a maximum 3% higher also than that of PP1. The post-stall performance is better for PP2 than for the other two models.

In this reference condition, the results of adding a serrated leading edge to a flat plate are mixed. The small serrations of PP3 have a mostly negative effect on the performance. This result differs from the observations of Cranston et al (2012) where, at a Reynolds number of 140,000, the small serrated plate had performance very similar to the basic flat plate. However, we must be careful when comparing to the experiments of Cranston et al (2012) because the relative amplitude of the serrations is different ( $(A/c)_{Cranston} = 1.5\%$  while  $(A/c)_{PP3} = 5\%$ ) and the Reynolds number is different. Moreover, Cranston et al (2012) takes into account three dimensional effects of tip vortices, while this is not the case in this study.

The medium serrations of PP2 delay stall and slightly enhance the maximum lift-to-drag ratio. The wavelength of the serrations tend to be an important parameter in the efficiency of the serrations. This result is consistent with what had been observed on different configurations of serrated leading edge in the previous studies by Hansen et al (2011) or Goruney and Rockwell (2009). They insisted on the importance of the ratio  $\lambda/A$  in the efficiency of the device. Here, the effect of this parameter is fully contained in the wavelength because the amplitude is kept constant in this study.

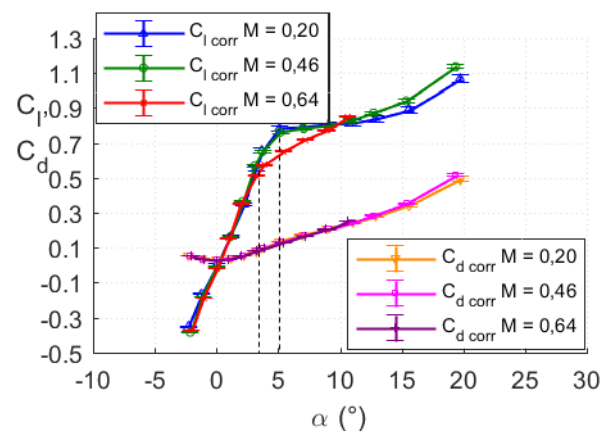


Fig. 9 Compressibility effect on PP1

4.1.2 Compressibility effect

The effects of compressibility are presented in Figure 9 and Figure 10 on PP1 and PP2, respectively.

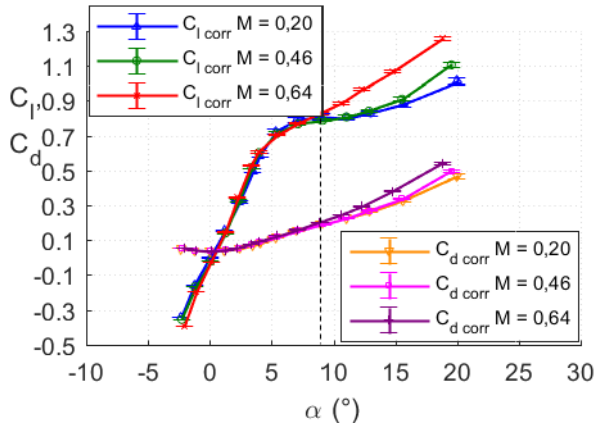


Fig. 10 Compressibility effect on PP2

The shapes of the lift and drag curves of PP3 are similar to those of PP2 and thus are not displayed here. It is worth noting that the lift curves at  $M = 0.64$  differ quite considerably from the two other conditions. Indeed, there is no real stall with a plateau of constant lift, here “stall” is merely a change in slope in the lift curves.

Then, while the lift coefficient is increasing when the Mach number increases in the deep stall condition at angles of attack higher than  $9^\circ$ , it is reduced at around stall angle. This effect tends to be more significant for the basic flat plate than for the models with serrations. Indeed, the stall angle moves from  $5^\circ$  to  $4^\circ$  on PP1 and the lift coefficient is much lower at  $5^\circ$  in the condition 3 than in the other conditions. This effect is far less significant on PP2 and PP3; the lift coefficient remains very similar to other Mach number conditions of  $\alpha \leq 9^\circ$  for both models.

For all the models, drag polars, not shown here, are quite insensitive to compressibility at the angle less than the stall angle. Around the stall angle, drag is increasing slightly with increasing the Mach number except for PP1 for which the increase is quite substantial. On the contrary after the stall, increasing the Mach number leads to decrease in the drag coefficient under the constant lift coefficient conditions.

Lift-to-drag ratio curves are not shown here but the main effects of compressibility are the following: PP1 has a sizeable, and early, spike in lift-to-drag ratio in the condition 3. The maximum lift-to-drag ratio is observed at an angle of attack of  $2^\circ$  instead of  $3.2^\circ$  in the two other conditions. PP2 and PP3 also show an earlier maximum in the condition 3 but the increase in  $L/D$  maximum value is much less important. For PP2 there is even no increase at all. What might be interesting with the latter is that the performance seems less impacted by compressibility: the variations in  $L/D$  ratio are small ( $L/D$  at  $4^\circ$  in condition 2 is 5% lower than in condition 1 and in the condition 3 it is 5.4% lower than in reference case).

The maximum of lift-to-drag ratio is obtained for a lower angle of attack with the increasing Mach number

for all the models we investigated. Furthermore, the Mach number does not affect the slope of the lift curve at angles of attack lower than the stall angle. Finally, the Mach number does not alter the lift coefficient of serrated plates below the angle of attack of the deep stall condition, while the basic flat plate suffers a significant decrease in the lift coefficient around the stall angle when the Mach number increases. Serrations tend to enhance the lift coefficient when the Mach number varies.

#### 4.2 PSP experiments

First, the pressure distribution does not appear to be symmetric on the three models equipped with pressure tubes. The flow is perturbed by the presence of the pressure tube under the wing. The extent of the alteration of the pressure distribution that ensues has been evaluated by comparison with a flat-plate model not equipped with pressure tube (PP4). By comparing chordwise  $C_p$  distributions, it has been determined that the pressure distribution on the half-span far from the tube is not affected, as shown on Figure 4. In this figure, the offset of the pressure distribution (usually obtained by pressure tap measurement) of PP4 has been determined by matching one point (designated by a red point in Figure 3) of the distribution with one on the distribution of PP1. A visual analysis of all the pressure distributions in all the cases tends to confirm this observation. So, the results presented later are PSP images of the half-span where the flow is not affected by the pressure tube disturbance. It should be noted that near the walls the flow is altered by the three-dimensional flow induced by the presence of the wall boundary layer. The portions of the wing where the flow is altered by these boundary layers have been greyed out. The analysis of the flow will focus on the part not affected by this disturbance.

##### 4.2.1 Flow structure on serrated flat plates at $M = 0.2$ and $Re = 12,000$

Several  $C_p$  distributions on PP2 in this condition at different angles of attack are presented in Figure 11. The flow structure resembles a small separation bubble (for  $\alpha > 0^\circ$ ) but there is also a spanwise pattern: each trough corresponds to a low pressure region and each peak a higher pressure area. This pattern is obtained for all angles of attack below  $6^\circ$ . On PP3, it is obtained for angles of attack less than  $4^\circ$ .

##### 4.2.2 Flow structure on serrated flat plates at $M = 0.46$ and $Re = 11,000$

Several  $C_p$  distributions on PP2 in this condition at different angles of attack are presented in Figure 12.

In this condition, two distinct flow patterns can be observed on PP2:

- For angles of attack less than  $6^\circ$ , the same flow pattern as in the condition 1 is obtained. It is highlighted at  $\alpha$

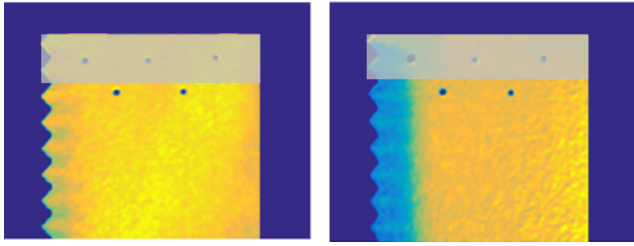


**Fig. 11**  $C_p$  distribution on PP2 at  $M = 0.2$ ,  $Re = 12,000$  (Condition 1) at  $\alpha = 0^\circ$  (left) &  $\alpha = 5^\circ$  (right). Colors correspond to the colorbar of Figure 13a.

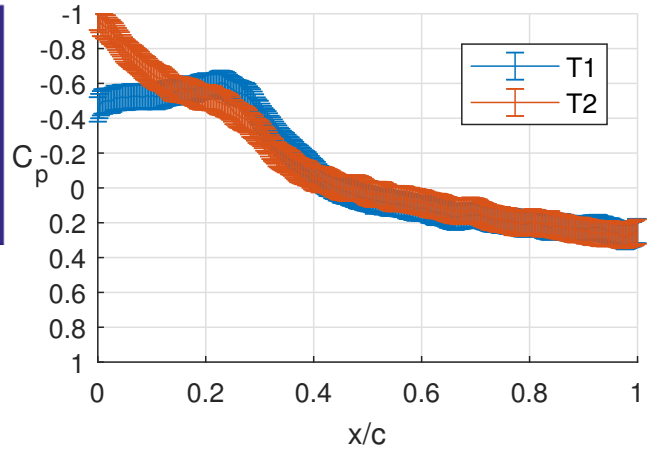
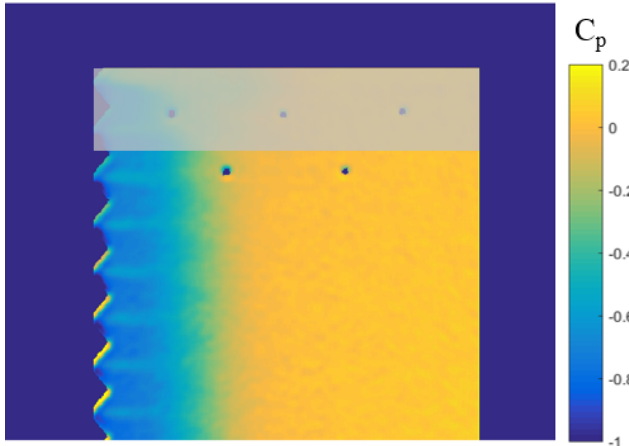
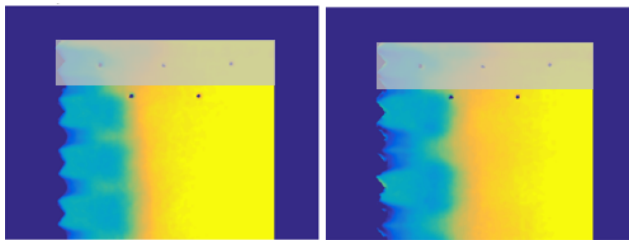


**Fig. 13** Chordwise  $C_p$  distribution in troughs T1 and T2 on PP2 at  $\alpha = 7^\circ$  and  $M = 0.46$



(a)  $\alpha = 4^\circ$



(b)  $\alpha = 6^\circ$  (left) &  $\alpha = 7^\circ$  (right)

**Fig. 12**  $C_p$  distribution on PP2 at  $M = 0.46$ ,  $Re = 11,000$  (Condition 2)

=  $4^\circ$  in [Figure 12\(a\)](#). To give an order of magnitude, at this angle of attack, the value of  $C_p$  is approximately -0.7 in low pressure areas.

- For angles of attack of  $6^\circ$  and higher, several troughs correspond to low pressure areas while others correspond to the relatively high pressure region similar to the peaks. To give an order of magnitude, on PP2 at  $\alpha = 7^\circ$ , the value of  $C_p$  is approximately -0.9 in the former ones and -0.6 in the latter ones as can be seen in Figure 4.2.2. This sort of pattern does not occur in the condition 1 while in the condition 3 it appears earlier. In the condition 2, there is no clear periodicity at  $\alpha \geq 9^\circ$  and then, the flow is completely detached at  $\alpha \geq 15^\circ$ . This flow pattern is not unique: the periodicity, as well as the size of the low pressure areas, varies with the angle of attack and the Mach number.

On PP3 a third flow pattern can be observed at  $\alpha = 11^\circ$  and  $\alpha = 15^\circ$ . The size of low pressure areas rises continuously from the centre of the wing towards the tip giving to the flow a global symmetry on the whole wing. This peculiar flow configuration is better seen at  $M = 0.64$ , and it is shown on PP2 in [Figure 14](#). In this image, the full-span pressure distribution is presented as the flow appears to be largely symmetric in spite of the presence of the pressure tube.

#### 4.2.3 Flow structure on serrated flat plates at $M = 0.64$ and $Re = 13,000$

Several  $C_p$  distributions on PP2 in this condition at different angles of attack are presented in [Figure 15](#).

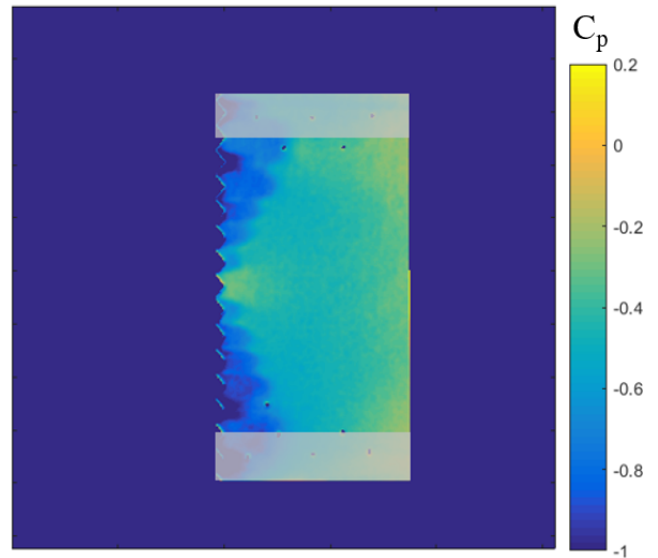


**Fig. 14** Flow configuration on PP2 at  $\alpha = 11^\circ$ ,  $M = 0.64$  &  $Re = 13,000$

In this condition the first flow pattern, as seen in [Figure 12\(a\)](#), is limited to  $\alpha = 0^\circ$  on both models. At

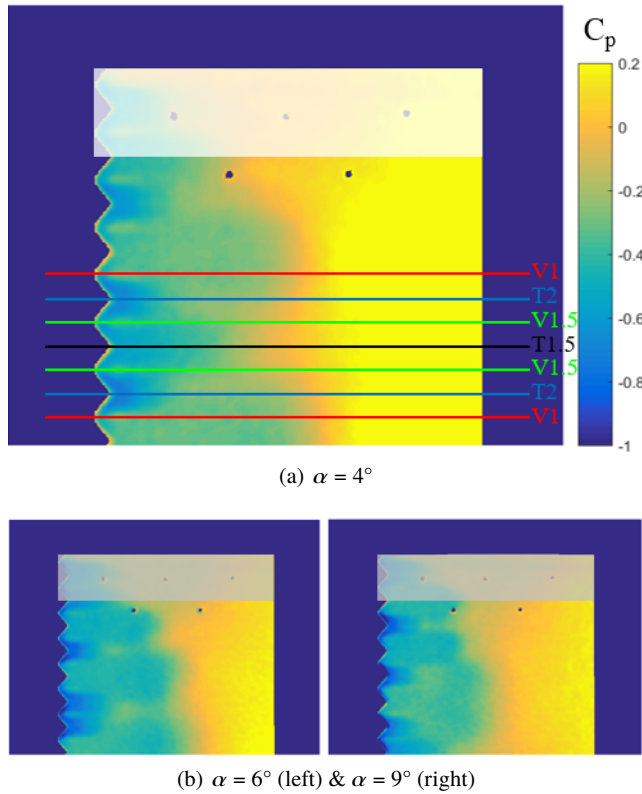


**Fig. 15**  $C_p$  distribution on PP2 at  $M = 0.64$ ,  $Re = 13,000$  (Condition 3)

$4^\circ \leq \alpha \leq 9^\circ$  the second pattern appears. Attached flows from several peaks are gathered downstream, enclosing small very low pressure areas. Other low pressure areas are much wider and expand until mid-chord or more, depending on the angle of attack.

At this Mach number both models feature the third type of flow configuration at  $\alpha = 11^\circ$ , shown in Figure 14, and  $\alpha = 15^\circ$ . Again, in this flow configuration, the pressure distribution is symmetric in spite of the presence of the pressure tube.

## 5 Flow categorisation

### 5.1 Three types of flow structures

Flow structures on flat plates with serrated leading edges can be divided into three main types of flow configuration. Those structures can be described as follows:

- The first flow type (FT1) is characterised by the presence of a low pressure area directly downstream of each trough, giving a flow periodicity equal to the leading-edge periodicity. Downstream of peaks the pressure is higher, pointing towards those regions remaining attached while low pressure areas after troughs face a stronger pressure recovery and might be separated. This is consistent with what has been hypothesised previously (Johari et al, 2007; Van Nierop

et al, 2008) and calculated by Dropkin et al (2012).

A schematic of this flow pattern is presented in

Figure 16(a).

- The flow type 2 (FT2) is characterised by the loss of the simple periodicity equal to the wavelength of serrations. Two types of low pressure areas appear downstream of troughs, the very low pressure (VLP) areas and the low pressure (LP) areas. Those areas tend to correspond to what Sakai et al (2015) called “closed” and “open” reverse-flow regions, respectively. The open reverse-flow areas are zones enclosed by merging flows coming from the peaks, while open reverse-flow areas are not enclosed by such flows. Hence, troughs and peaks can be classified with the categorisation by Sakai et al (2015): T1 refers to troughs which are followed by a low pressure area and T2 to those followed by a very low pressure area. V1 peaks which are located in between T1 and T2 and the flow downstream of those peaks is curved. V2 peaks are located in between two T2 troughs and the flow downstream continues straight. Figure 16(b) presents an example of such a categorisation. On PP2, at a Mach number of 0.64, the pressure distributions at several angles of attack also feature intermediate low pressure regions with a pressure lower than that in LP areas and higher than that in VLP regions. Intermediate pressure areas are also characterised by a length that is lower than the one of LP areas but larger than the one of VLP areas. T1.5 troughs and V1.5 peaks could be defined as troughs upstream of intermediate pressure areas and peaks between VLP regions and intermediate pressure areas. These pressure distributions can be observed in Figure 15(a). The periodicity of the pattern depends on the angle of attack and the Mach number, as well as on chordwise location. A complete analysis of the periodicity is presented in subsection 5.2.

- The third type of flow structure (FT3) is characterised by a global symmetry of the flow on the wing. The same types of pressure areas as in FT2 can be found. However, in this case the size of low pressure areas rises continuously from the mid-span towards the tip of the wing.

In order to better describe each flow type, it is interesting to plot chordwise  $C_p$  curves in troughs and peaks. The shape of those curves varies depending on the flow type. An example of the  $C_p$  curves obtained on different troughs and peaks is shown in Figure 17.

The analysis of all the cases allows highlighting characteristic shapes of  $C_p$  curves at trough locations and peak locations for each flow type. Characteristics shapes of  $C_p$  curves in FT1 are plotted in Figure 18. At trough locations the  $C_p$  curves feature a low  $C_p$  in the trough and a linear pressure recovery while at peaks locations there is a plateau in the pressure recovery corresponding to the attached flow downstream of the peaks.  $C_p$

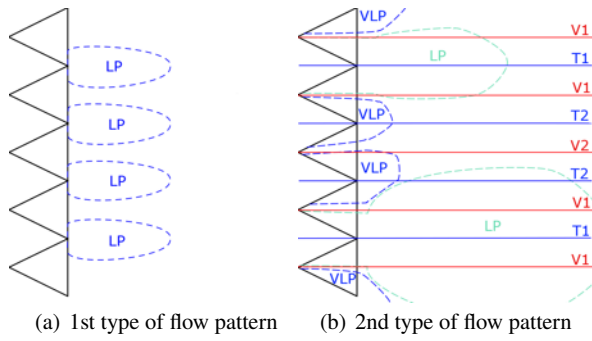


**Fig. 16** Two types of flow patterns observed at  $M = 0.46$  and  $Re = 11,000$ . VLP stands for very low pressure and LP for low pressure

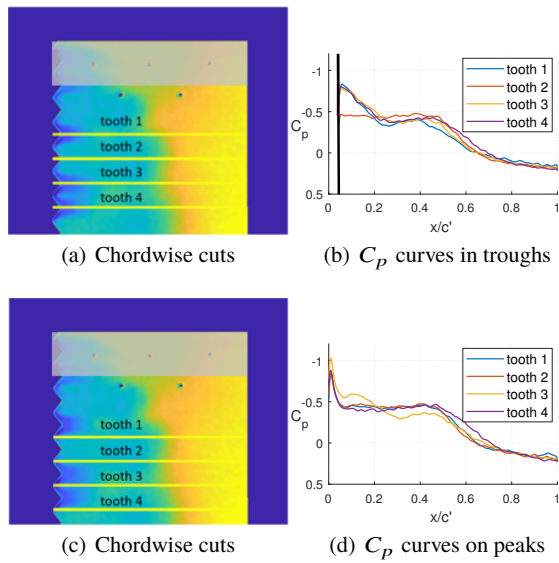
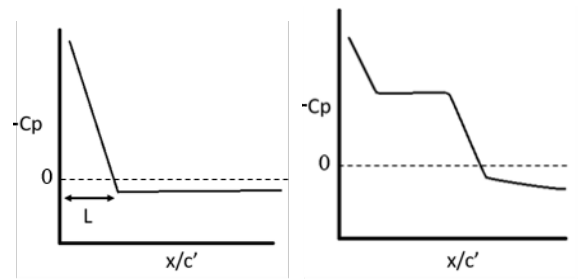


**Fig. 17**  $C_p$  curves on PP2 at  $M = 0.64$  and  $\alpha = 6^\circ$

curves shapes in FT2 are presented in [Figure 19](#) and  $C_p$  curves shapes in FT3 are displayed in [Figure 20](#). In [Figure 18](#),  $L$  depends on serration wavelength and slightly on the Mach number. In [Figure 19](#),  $L$  increases when the Mach number increases. This length depends on serrations wavelength; it does not vary significantly with spanwise location. In [Figure 20](#),  $L$  varies with the spanwise location, decreasing towards the centre of the wing. Also,  $L$  decreases with the increasing angle of attack as the size of the low pressure region decreases.

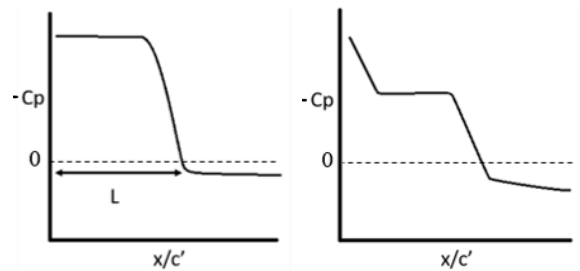
It can be found that if the schematic shapes of the  $C_p$  curves might be the same in different flow types, the combination of trough and peak  $C_p$  curves gives quite a good characterisation of each flow structure. Here, FT1 is well identified, as well as the different types of troughs and peaks of FT2. Also, FT3 being defined by a trend in the size of flow structures similar to those observed in FT2, it is not surprising that the shapes of the  $C_p$  curves are similar. It is the variation of  $L$  that characterises this flow type. Those  $C_p$  curves provide a local characterisation of the different types of flow, complementary to

the global characterisation that has been performed by observing the two-dimensional  $C_p$  distributions.

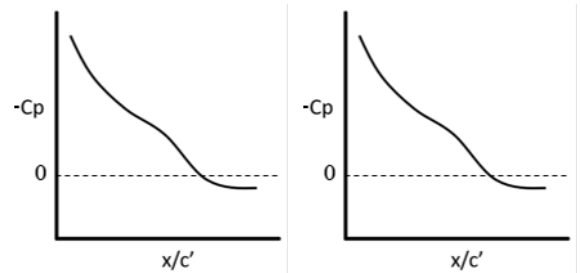


(a)  $C_p$  curves shape at troughs locations (b)  $C_p$  curves shape at peaks locations

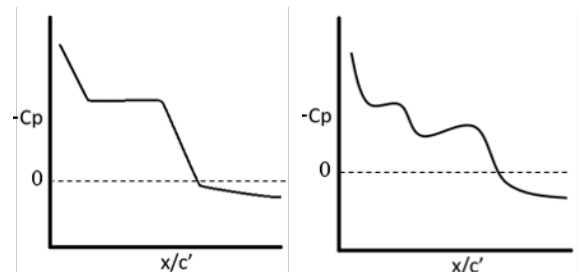
**Fig. 18**  $C_p$  curves shapes in FT1



(a)  $C_p$  curves shape at T1 troughs locations (b)  $C_p$  curves shape at V1 peaks locations



(c)  $C_p$  curves shape at T1.5 troughs locations (d)  $C_p$  curves shape at V1.5 peaks locations



(e)  $C_p$  curves shape at T2 troughs locations (f)  $C_p$  curves shape at V2 peaks locations

**Fig. 19**  $C_p$  curves shapes in FT2

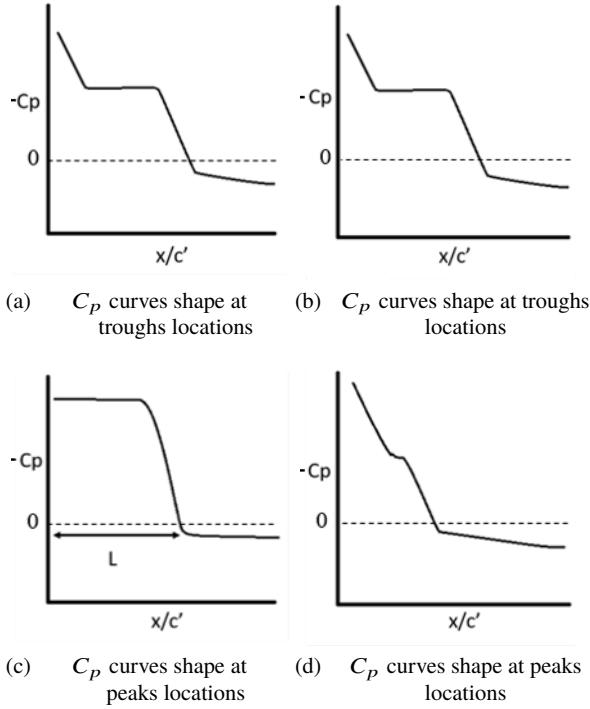


Fig. 20  $C_p$  curves shapes in FT3

## 5.2 Periodicity analysis

In order to further describe the flow over serrated flat plates, an analysis of the periodicity of spanwise  $C_p$  distributions has been carried out. The principle of the study is presented in Figure 21. To obtain the appropriate discrete Fourier transform results, the flow is supposed to be symmetric and a symmetry is applied to the part of the flow not disturbed by the pressure tube. In order to avoid wall interference in the  $C_p$  curves, the area of the  $C_p$  distribution used for the analysis has been limited to the centre of the flow. The result of the analysis is the single-sided power spectral density spectrum (PSD) presented here in semi-logarithmic axes. In this plot, the frequency has been normalised by the wave number of serrations  $f/\lambda = 1/\lambda$ . Due to the hypothesis of the flow symmetry, there is a rise in PSD value at low frequency, it is not taken into account in the discussion of the flow mechanisms presented in subsection 5.3.

Several results of the periodicity analysis for PP3 are summarised in Figure 22. The legend presented in Figure 22(c) is the same for all the graphs.

In Figure 22 the different flow types have been located. FT1 is characterised by its simple  $\lambda$ -periodicity. FT2 is characterised by the variety of periods that can be observed, between  $\lambda$  and  $7\lambda$  for PP3 and  $\lambda$  and  $4\lambda$  for PP2. As the flows coming from different peaks merge after the very low pressure areas. Concomitantly, the low pressure areas spanwise size tend to increase with chordwise position. These two observations explains the variety of

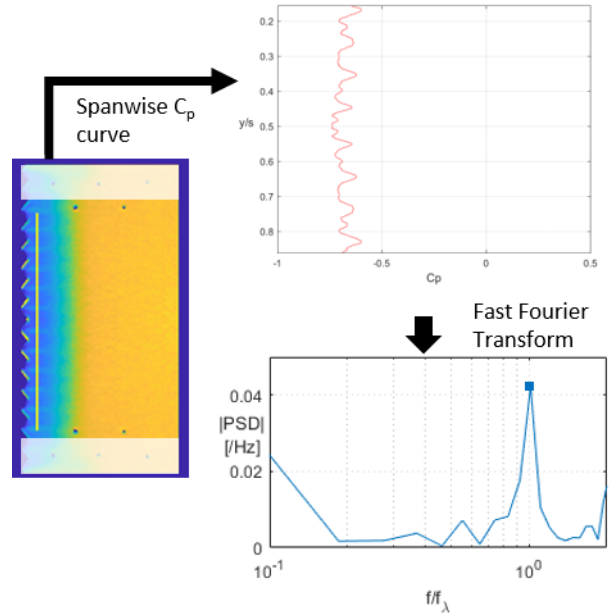


Fig. 21 Periodicity analysis principle on PP2 at  $M = 0.46$ ,  $\alpha = 4^\circ$  and  $x/c' = 0.1$

periods observed and their increase with chordwise position. In FT2 the period increases with increasing angle of attack. When the frontier with FT3 is reached, the period decreases suddenly from  $7\lambda$  to  $2-4\lambda$  for PP3. In Figure 22(a), it can be found that, at  $\alpha = 4-5^\circ$  at  $M = 0.2$ , a  $2\lambda$  period is appearing. This is the frontier between FT1 and FT2.

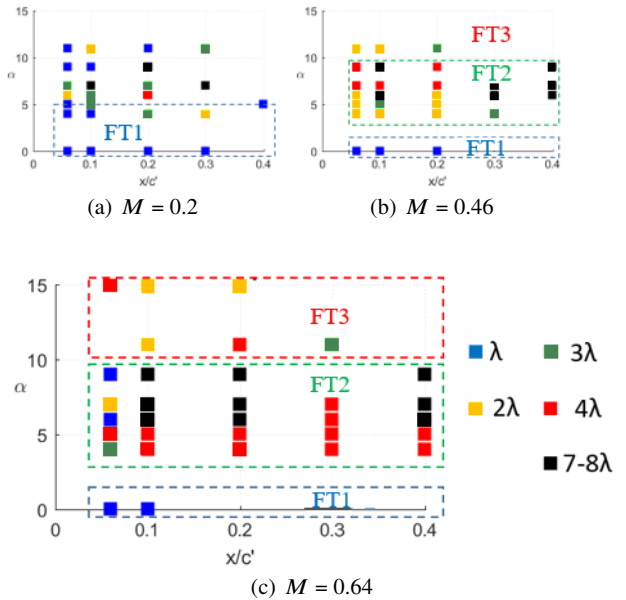


Fig. 22 Period map of PP3 at different Mach numbers

The different analyses allow to plot, for each model, a map specifying the type of flow depending on the angle of attack and the Mach number. To create these maps, each case was associated, when possible, to a flow type by vi-

sual observation of the pressure distribution. Then the two other analysis methods (chordwise  $C_p$  curves shapes and periodicity analyses) were conducted and results were found to be consistent with the first categorisation, giving more confidence in this one. These maps for PP2 and PP3 are presented in Figure 23. Dashed lines are limits that would require more data to be set accurately and which shape is not known, in particular in the low Mach number region. There is a significant uncertainty about the position of the FT2 limits which are not completely determined. FT2 has not been clearly observed at low Mach number in this study but was described previously by Sakai et al (2015).

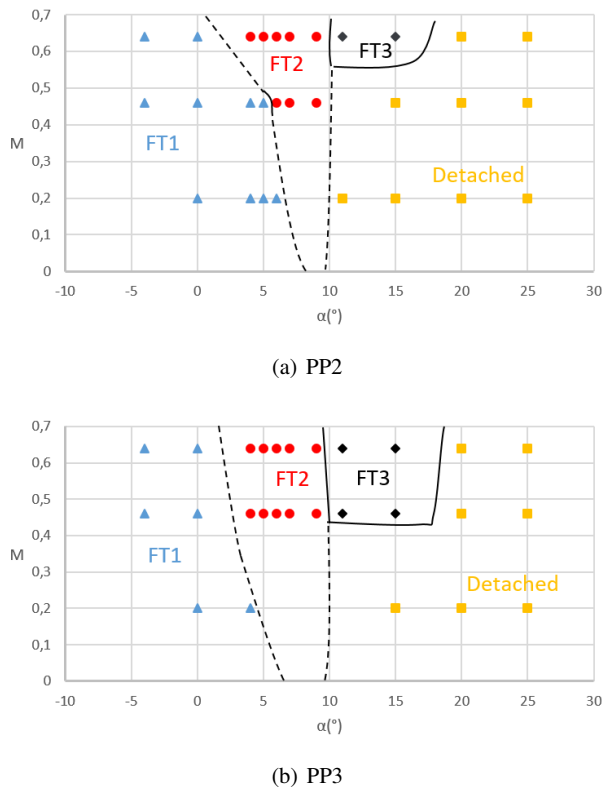


Fig. 23 Flow type maps

### 5.3 Flow mechanisms

As it has been noticed in subsection 5.1, FT1 and FT2 are similar to the flow configurations studied by Sakai et al (2015). In that paper, they used PIV to study the velocity field on serrated flat plates. The results of the present study are consistent with theirs, thus their flow structure categorisation has been reused. In FT1, which corresponds to their case at  $\alpha = 6^\circ$ , their reverse-flow regions downstream of troughs correspond to the low pressure regions that have been observed in the present study. Their explanation for the flow mechanism in this case is consistent with our results. Each low pressure region corresponds to counter-rotating vortices, with an upward velocity downstream of troughs and a downward

one downstream of peaks. This tends to be coherent with the lower pressure in troughs and the higher one on peaks. Thus, one of the schematics presented by Sakai et al (2015) is completed with the location of low pressure areas in Figure 24. This consistency also allows completion of our schematic of FT1 with the velocity field described by Sakai et al (2015) in Figure 25(a). The flow over the peaks continues straight between the low pressure areas.

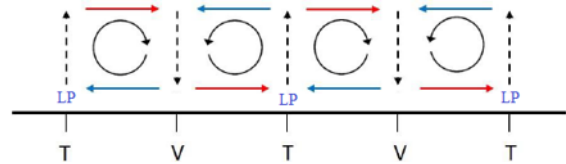


Fig. 24 Vortical structures inside low pressure areas in FT1 (based on Sakai et al (2015))

In FT2, which corresponds to their case at  $\alpha = 14^\circ$ , the "open" reverse-flow regions that they describe tend to correspond to the low pressure regions of our flow, while the "closed" reverse-flow areas correspond to the very low pressure zones of our flow. Also in this case, the flow mechanism described by Sakai et al (2015) is consistent with our results. Counter-rotating vortices have been observed in the very low pressure areas. These vortices move upward when they encounter the relatively higher pressure of the low pressure areas. The very low pressure areas are thus "blocked" in their development by the low pressure ones. The intermediate pressure zones that have been found at several angles of attack are also smaller than the low pressure areas and might also be constrained by the latter ones. However, as no PIV study of these regions has been conducted, the presence of vortices cannot be ascertained, and the flow mechanism in those areas remains unknown. Nevertheless, in the basic FT2, the consistency of our observation with the work of Sakai et al (2015) allows completion of our schematic of FT2 with the velocity field that they describe in Figure 25(b). The flow on V1 peaks, between T1 and T2 troughs (thus between very low and low pressure regions), is curved while the flow on V2 peaks between two T2 troughs is straight.

FT3 has not been described by Sakai et al (2015), no previous observation of such a flow structure has been found. Its flow structures are similar to those of FT2, however the trend in the low pressure areas size is a new feature. In FT2, when increasing the angle of attack, the length of the low pressure areas increases from  $\lambda$  to approximately  $8\lambda$  with the most common wavelengths being  $\lambda, 2\lambda, 4\lambda, 8\lambda$ . By extrapolating this tendency, we could expect that the next wavelengths reached would be  $16\lambda$  and  $32\lambda$  which on PP3 correspond to the wing-span. If the wavelength reached this value, the centre of the wing could correspond to a node while the wing tips could correspond to anti-nodes, thus explaining the flow configuration and the evolution of  $L$  with the spanwise

location in FT3. This reasoning would require further investigations to be asserted. Furthermore, observing that in FT3, contrary to FT2, the flow is never recompressed and thus stays detached, a flow mechanism is proposed hereafter.

The structure of the flow might originate in the burst of a low pressure area that would never reattach. This low pressure area would limit the extent of the intermediate and very low pressure areas located downstream of troughs. The decrease in the size of those areas with increasing angle of attack would be explained by the increase in the size of the burst “bubble.” When this burst bubble would reach the leading-edge, the flow on the entire wing would be detached. Figure 26 displays a FT3 picture where the limits of the different types of low pressure bubbles are outlined. The very low pressure areas are circled in red, the intermediate pressure areas in green and the burst low pressure region in black.

This explanation is only partial and cannot be proved with the data of this study. Why FT3 occurs remains an open question that need further investigations. In particular experiments with other measurement methods to access the velocity field might be helpful to understand the flow mechanisms.

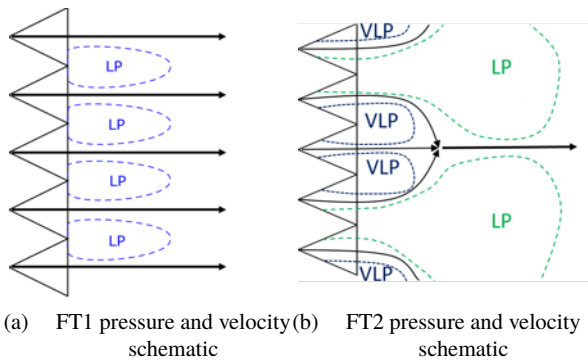


Fig. 25 Schematics of flow structures of FT1 and FT2

## 6 Conclusion

Aerodynamic performance and pressure distributions on serrated leading-edge flat plates in low-Reynolds-number and subsonic high-Mach-number conditions have been investigated. The results can be summarised as follows:

- Aerodynamic performance of flat plates with leading-edge serrations are almost the same as those of a standard flat plate. PP2 displays slight enhancements of performance at around the stall angle compared to the reference flat plate while PP3 has a worse performance throughout.
- The Mach number does not affect the slope of the aerodynamic lift at an angle of attack below the stall angle. It also does not alter the lift coefficient of serrated plates unless it is in a deep stall condition while

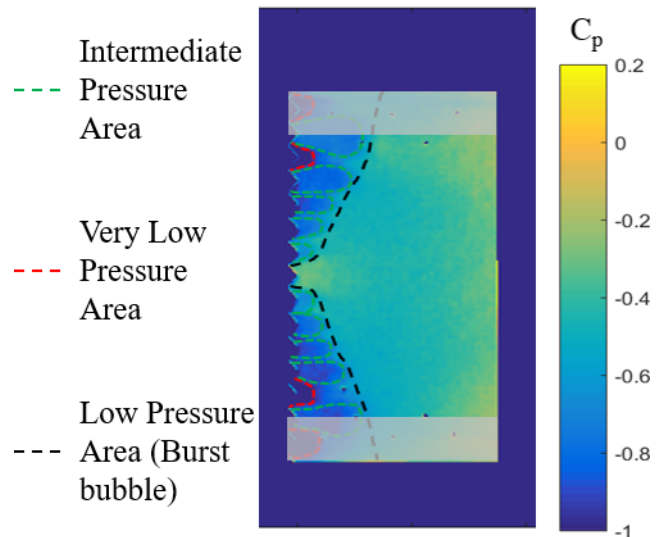


Fig. 26  $C_p$  distribution with outline of pressure areas in FT3

the basic flat plate suffers a significant decrease in the lift coefficient around stall when the Mach number increases. Serrated models tend to be less sensitive to Mach number variations.

- The flow on serrated flat plates is generally organised with low pressure regions downstream of troughs where the flow encounters a steeper pressure gradient than downstream of peaks.
- Three different types of flow configuration have been observed. These configurations feature two different main types of low pressure regions and various values of periodicity of the pattern. This categorisation has been supported by two-dimensional  $C_p$  distributions, chordwise local  $C_p$  curves and spanwise  $C_p$  periodicity analyses.
- This work can be related to the study of Sakai et al (2015). The same kind of flow configuration has been observed, with the present study emphasising the importance of the Mach number as well as angle of attack in the establishment of this flow configuration. The studies have been found to be consistent.

**Acknowledgements** This work has been carried out in the framework of the exchange agreement between ISAE-SUPAERO and Tohoku University. First author E.M. would like to thank Shintaro Ando for assisting in experiments.

## References

- Anyoji M (2011) Development of a mars wind tunnel and its applications to low reynolds number and high-subsonic airfoil testing. PhD thesis, Tohoku University Graduate School of Engineering
- Anyoji M, Nagai H, Asai K (2009) Development of low density wind tunnel to simulate atmospheric flight on mars. 47th AIAA Aerospace Sciences Meeting including The New Horizons Forum and Aerospace Exposition AIAA paper 2009-1517
- Anyoji M, Numata D, Nagai H, Asai K (2015) Pressure-sensitive paint technique for surface pressure measurements in a low-density wind tunnel. Journal of Visualization 18(2):297–309
- Cranston B, Laux C, Altman A (2012) Leading edge serrations on flat plates at low reynolds number. 50th AIAA Aerospace Sciences Meeting including the New Horizons Forum and Aerospace Exposition AIAA paper 2012-0053

- Custodio D (2007) The effect of humpback whale-like leading edge protuberances on hydrofoil performance. PhD thesis, Worcester Polytechnic Institute
- Dropkin A, Custodio D, Henoch C, Johari H (2012) Computation of flow field around an airfoil with leading-edge protuberances. *Journal of Aircraft* 49(5):1345–1355
- Goruney T, Rockwell D (2009) Flow past a delta wing with a sinusoidal leading edge: near-surface topology and flow structure. *Experiments in Fluids* 47(2):321–331
- Guynn M, Croom M, Smith S, Parks R, Gelhausen P (2003) Evolution of a mars airplane concept for the ares mars scout mission. 2nd AIAA Unmanned Unlimited Conf and Workshop & Exhibit AIAA paper 2003-6578
- Hansen KL, Kelso RM, Dally BB (2011) Performance variations of leading-edge tubercles for distinct airfoil profiles. *AIAA Journal* 49(1):185–194
- Johari H, Henoch CW, Custodio D, Levshin A (2007) Effects of leading-edge protuberances on airfoil performance. *AIAA Journal* 45(11):2634–2642
- Laitone E (1997) Wind tunnel tests of wings at reynolds numbers below 70 000. *Experiments in Fluids* 23(5):405–409
- Liu T, Sullivan J (2005) Pressure-and Temperature-Sensitive Paints. Wiley Online Library
- Miklosovic D, Murray M, Howle L, Fish F (2004) Leading-edge tubercles delay stall on humpback whale (megaptera novaeangliae) flippers. *Physics of fluids* 16(5):L39–L42
- Mori H, Niimi T, Oshima Y, Hirako M (2004) Development of pressure sensitive paint suitable to surface pressure measurement in high-knudsen number flows. *Transactions of the Japan Society of Mechanical Engineers Part B (Japan)* 16(11):2721–2728
- Okamoto M, Yasuda K, Azuma A (1996) Aerodynamic characteristics of the wings and body of a dragonfly. *Journal of Experimental Biology* 199:281–294
- Oyama A, Fujii K (2006) A study on airfoil design for future mars airplane. 44th AIAA Aerospace Sciences Meeting and Exhibit AIAA paper 2006-1484
- Pankhurst RC, Holder DW (1952) *Wind-tunnel technique: an account of experimental methods in low-and high-speed wind tunnels*. Pitman
- Sakai M, Sunada Y, Rinoie K (2015) Three-dimensional separated flow on a flat plate with leading-edge serrations. 53rd AIAA Aerospace Sciences Meeting AIAA paper 2015-0047
- Sun J, Bhushan B (2012) The structure and mechanical properties of dragonfly wings and their role on flyability. *Comptes Rendus Mécanique* 340(1-2):3–17
- Van Nierop EA, Alben S, Brenner MP (2008) How bumps on whale flippers delay stall: an aerodynamic model. *Physical Review Letters* 100(5):054,502
- Yamashita T, Sugiura H, Nagai H, Asai K, Ishida K (2007) Pressure-sensitive paint measurement of the flow around a simplified car model. *Journal of Visualization* 10(3):289–298